



Lunar deep materials observed by Chang'e-4 rover

Sheng Gou^{a,b}, Kaichang Di^{a,b,c}, Zongyu Yue^{a,c,*}, Zhaoqin Liu^a, Zhiping He^d, Rui Xu^d, Honglei Lin^e, Bin Liu^{a,b}, Man Peng^a, Wenhui Wan^a, Yexin Wang^a, Jianzhong Liu^f

^a State Key Laboratory of Remote Sensing Science, Institute of Remote Sensing and Digital Earth, Chinese Academy of Sciences, Beijing 100101, China

^b State Key Laboratory of Lunar and Planetary Sciences, Macau University of Science and Technology, Macau, China

^c CAS Center for Excellence in Comparative Planetology, Hefei 230026, China

^d Key Laboratory of Space Active Opto-Electronics Technology, Shanghai Institute of Technical Physics, Chinese Academy of Science, Shanghai 200083, China

^e Key Laboratory of Earth and Planetary Physics, Institute of Geology and Geophysics, Chinese Academy of Sciences, Beijing 100029, China

^f Institute of Geochemistry, Chinese Academy of Sciences, Guiyang 550002, China

ARTICLE INFO

Article history:

Received 8 May 2019

Received in revised form 2 September 2019

Accepted 9 September 2019

Available online xxx

Editor: F. Moynier

Keywords:

Chang'e-4 rover

in-situ observations

regolith and rock fragment

lunar mantle materials

differentiated melt pool

ABSTRACT

China's Chang'e-4 spacecraft achieved the first ever soft-landing within the South Pole-Aitken (SPA) basin on the farside of the Moon. The Chang'e-4 rover, named Yutu-2, made in-situ spectral observations on lunar regolith and a rock fragment at 11 locations during a nominal three-month mission period. The lunar regolith has a relative high olivine/pyroxene ratio, with the pyroxene being chiefly Mg-rich Low-Ca pyroxene (LCP). The rock fragment has a similar Mg-rich composition to that of the regolith. According to the surrounding topographic and geologic context, though originating from the lower base of a differentiated melt pool cannot be excluded here, the rover observed regolith and rock fragment are very likely to be lunar mantle materials excavated from nearby Finsen crater.

© 2019 Elsevier B.V. All rights reserved.

1. Introduction

Chang'e-4 successfully landed in Von Kármán crater inside the South Pole-Aitken (SPA) basin on January 3, 2019 (Li et al., 2019), marking the first soft landing of human spacecraft on the farside of the Moon. The SPA basin is the largest (~2500 km in diameter), oldest (Pre-Nectarian, formed between ~3.8 and ~4.3 Ga ago) and deepest (~13 km deep) recognized impact basin on the Moon (Stuart-Alexander, 1978; Spudis et al., 1994). Several studies have suggested the SPA-forming impact was perhaps very oblique. The identified evidences include elliptical ring structures (Garrick-Bethell and Zuber, 2009), an observed Fe anomaly and Th enhancement within the basin interior (Lawrence et al., 1998), and a far offset between the SPA antipode and the nearside center of the lunar mare concentrations (Schultz and Crawford, 2011). These evidences suggest the SPA impact would not have excavated as deep into the lunar interior, maybe only excavating shallowly into the lunar crust, which is even favored by observations of the feldspathic ejecta of SPA. However, according to the numerical impact

simulations, lunar mantle material should be excavated by some of the largest lunar impact events (Miljkovic et al., 2015). Melosh et al. (2017) showed that, even in the most conservative simulation case of a 200-km-diameter impactor striking the Moon at 45°, the SPA basin should have sampled the lunar lower crust and upper mantle to a maximum excavation depth of 105 km. Zhu et al. (2018) showed in the case of a 630-km-diameter impactor with an impact velocity of 18 km/s hitting the Moon at an angle of 20° produces a transient cavity with a diameter of ~1400 km, excavates up to a depth of ~140 km and exposes the mantle within the basin.

The ~186 km diameter pre-Nectarian Von Kármán crater lies in the northwestern portion of the Mg-Pyroxene Annulus of the SPA basin (Stuart-Alexander, 1978; Moriarty and Pieters, 2018), and pre-impact crust beneath Von Kármán is likely to have already been thinned by the SPA impact. The estimated approximate impact excavation and melting depth Hexc of Von Kármán crater is 9.3–12.05 km, which is calculated from the equation $Hexc \approx 0.05-0.065D$ (D is the final complex crater diameter) (Melosh, 1989). The newly acquired high-resolution gravity data from the Gravity Recovery and Interior Laboratory (GRAIL) mission showed Von Kármán crater has a relatively thin crust that is less than 5 km (Wieczorek et al., 2013). Von Kármán is thus one candidate crater, with an impact melting and central peak source depth

* Corresponding author at: State Key Laboratory of Remote Sensing Science, Institute of Remote Sensing and Digital Earth, Chinese Academy of Sciences, Beijing 100101, China.

E-mail address: yuezy@radi.ac.cn (Z. Yue).

clearly exceeding the modeled lunar crustal thickness, to investigate possible excavated mantle materials. The interior of Von Kármán was heavily bombarded by numerous impacts and subsequently flooded with one or several periods of basalt flows and the ejecta from the nearby craters during the Imbrian period (Huang et al., 2018), which have greatly modified the topography and surface compositions. In order to have the maximum likelihood of conducting in-situ observations on the occurrence of deep seated, possibly mantle-derived materials within Von Karman crater, Chang'e-4 landed on the relatively smooth mare basalt plain emplaced at the south floor of the crater (Wu et al., 2019). Therefore, interpretations of the in-situ measured spectra, which is collected by the Visible and Near-Infrared Imaging Spectrometer (VNIS) onboard Chang'e-4 rover, should shed light on the mineralogical compositions of the possible lunar deep interior's materials that has long puzzled lunar geologists. For example, olivine is expected to be abundant in the lunar mantle, however, orbital spectral measurements have only found mere traces of olivine in limited places within SPA basin (Yamamoto et al., 2012). These results would thereby provide favorable or unfavorable evidences for previous suggestions on the compositions of the possible lunar deep materials excavated from the mantle.

This study analyzes characteristics of spectra collected by in-situ observations from VNIS during a nominal three-month mission period, and infers mineral compositions of the regolith and rock fragment at the Chang'e-4 landing site. Low band area ratio (BAR) values (0.27 ± 0.10) suggest a relatively high olivine/pyroxene ratio within local lunar regolith and rock fragment, and short 1000 nm and 2000 nm absorption centers (979.6 ± 15.5 nm and 1990.7 ± 35.0 nm, respectively) indicate pyroxenes are chiefly Mg-rich orthopyroxenes (low-Ca pyroxene, LCP). According to analysis on surrounding topography and geologic background, the Chang'e-4 landing site is on the ejecta of the ~ 72.98 km diameter Finsen crater, and it would make sense that the local lunar regolith and rock fragment be essentially composed of lunar upper mantle materials excavated from Finsen.

2. Spectrometers and spectral products

2.1. Description of VNIS

The Chang'e-4 mission includes a communication relay satellite, a lander, and a rover (Jia et al., 2018). Six scientific payloads have been installed on Chang'e-4 spacecraft to carry out planned objectives and tasks, with three payloads on the lander: the descent camera, the terrain camera, and the low frequency spectrometer, and three payloads on the rover (named Yutu-2): the panoramic camera, the lunar penetrating radar, and the Visible and Near-Infrared Imaging Spectrometer (Jia et al., 2018).

VNIS was designed and manufactured by Shanghai Institute of Technical Physics, Chinese Academy of Sciences. It's composed of a visible/near-infrared (VIS/NIR) imaging spectrometer, a short-wave infrared (SWIR) single-pixel non-imaging spectrometer, and a white panel for calibration and dust-proofing (He et al., 2014). The spectral range is 450–2395 nm with a default sampling interval of 5 nm, and the total spectral channels is 400 (100 channels from 450 to 945 nm for the VIS/NIR imaging spectrometer and 300 channels from 900 to 2395 nm for the SWIR spectrometer, with 10 overlap channels between 900–945 nm) (He et al., 2014). The VNIS is mounted at the front of the Yutu-2 rover and is inclined 45° from a height of 0.69 m above the lunar surface (He et al., 2014). VNIS is capable of synchronously acquiring the full spectrum of lunar surface objects and in-situ calibration. The effective pixels of the VIS/NIR imaging spectrometer are 256×256 , and the spatial resolution is about 1 mm/pixel. The field of view of the SWIR spectrometer corresponds to a circular region in the

VIS/NIR image with the center located at (96, 128) and a radius of 54 pixels (Supplementary Fig. 1) (He et al., 2014).

2.2. VNIS in-situ observations

Since the successful deploying on the lunar surface, the Yutu-2 rover has traversed 163 m (odometer reading) during a nominal three-month mission period and made in-situ observations using its suite of science instruments (Supplementary Table 1). These observations provide first-ever datasets to study the geomorphology, mineral composition, and subsurface structure within Von Kármán crater. VNIS made 14 in-situ observations of different targets at 11 sites along the rover traverse, including 13 observations for lunar regolith and 1 observation for a rock fragment (Supplementary Fig. 1).

3. Methods

3.1. Reflectance derivation

Details of processing and calibration for producing VNIS L2B spectral radiance data from original L0 data can be found in He et al. (2014) and Liu et al. (2013). The reflectance properties, which are crucial for mineral identification and quantification, are controlled by the physical and chemical state of the surface regolith, the surface roughness and the geometric circumstances (e.g. solar incidence angle). The L2B radiance data is firstly corrected by on-board radiometric calibration coefficients for both VIS/NIR and SWIR spectrometers in this study, which is provided by the VNIS manufacturer after on-board synchronous calibration experiments during the three lunar days. Reflectance (Bidirectional Reflectance Factor, BRF) is then derived by the solar irradiance calibration method (Eq. (1)) (Wu et al., 2018).

$$BRF(\lambda, \theta_i, \varphi_i, \theta_r, \varphi_r) = \frac{\pi \cdot I(\lambda, \theta_i, \varphi_i, \theta_r, \varphi_r) \cdot D^2}{E_0(\lambda) \cdot \cos(\theta_i)} \quad (1)$$

where λ , θ_i , φ_i , θ_r , and φ_r are the wavelength, solar zenith angle, solar azimuth angle, viewing zenith angle, and viewing azimuth angle, respectively. I is the VNIS L2B spectral radiance after radiometric correction. $E_0(\lambda)$ is the solar irradiance at 1 AU, which is adopted from Coddington et al. (2016) and resampled to VNIS spectral channels. D is the Sun–Moon distance in kilometers at the observation time divided by the standard Sun–Earth distance (149,597,870.7 km).

3.2. Spectrum discontinuity elimination

The VIS/NIR spectrum is derived firstly by averaging 9145 pixels in a circle area that corresponds to the field of view of the SWIR spectrometer (the center of the circle is located at (96, 128) of the VIS/NIR image and the radius is 54 pixels). The discontinuity at the boundary of derived average VIS/NIR spectrum and SWIR spectrum is clear, both for the calibration white panel and the target on lunar surface (e.g., regolith) (Fig. 1a). Typical average signal-to-noise ratios (SNR) of the derived VIS/NIR spectrum and SWIR spectrum that calculated from in-flight calibration are 37.4 dB and 44.0 dB, respectively. Average standard deviations of each measurement for VIS/NIR and SWIR channels are 2.3% and 2.7%, respectively, demonstrating absorption features with depth greater than 3% can be uniquely distinguished from the noise. Considering the SWIR spectrum has higher signal-to-noise ratio and stability, the derived VIS/NIR spectrum should be adjusted to the SWIR spectrum. There is no obvious slope difference on the overlapping 10 bands from 900 to 945 nm between the derived VIS/NIR spectrum and SWIR spectrum, thus there is only an offset between the

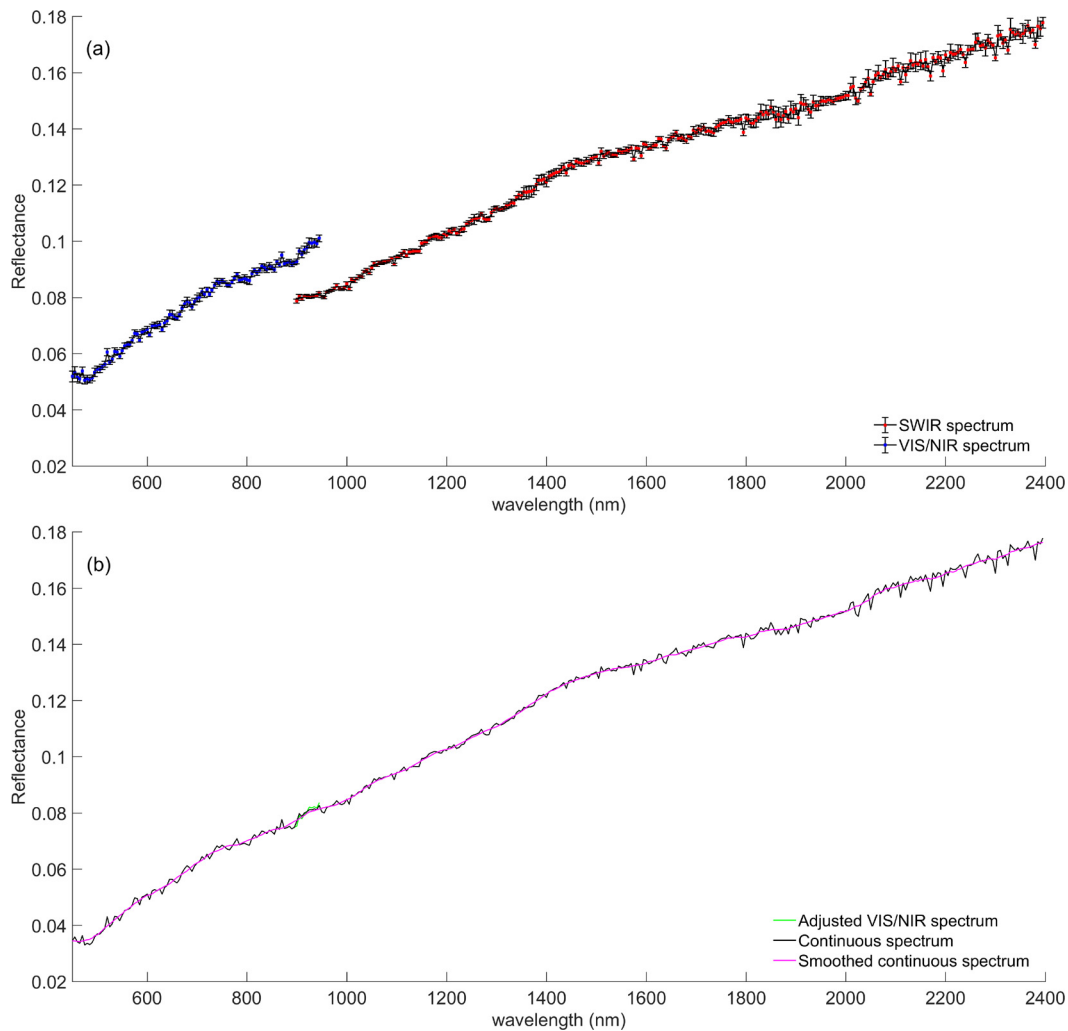


Fig. 1. The first in-situ observed spectrum on the lunar farside at site A. (a) Illustration of spectrum discontinuity; (b) Eliminating discontinuity and smoothing spectrum. The error bars in (a) represent standard deviation of each spectral channel. (For interpretation of the colors in the figure(s), the reader is referred to the web version of this article.)

two spectra. A linear regression fitting is applied on the overlapping bands between VIS/NIR and SWIR spectrum for the purpose of keeping the shape of the VIS/NIR spectrum. The equation has the form $Y = X + b$, where Y is SWIR spectrum, X is VIS/NIR spectrum, and b is the offset. The calculated offset is then added to the VIS/NIR spectrum and the mean spectrum value of the overlapping bands is also calculated to construct full-range continuous spectrum (Fig. 1b). The full-range continuous spectrum is further smoothed with a 3-point unweighted sliding-average algorithm to reduce noise before calculating spectral parameters (Fig. 1b).

3.3. Spectral parameter calculation

Absorption features are a function of mineralogy and their spectral shapes are controlled by chemical compositions, modal proportions, and space weathering. Pyroxene and olivine are major mafic minerals on planetary bodies, which are distinguished by their specific spectral characteristics. Pyroxene exhibits simple gaussian shaped absorption features at ~ 1000 nm and ~ 2000 nm, whereas olivine has three overlapping absorption features at approximately 850, 1050, and 1250 nm, forming what appears to be a single, broad, and composite absorption feature at ~ 1050 nm (Sunshine and Pieters, 1998). Plagioclase is also an important mineral component and has significant implications for the origin of the VNIS observed lunar regolith and rock fragment. Due to the incorporation of minor amounts of FeO (< 1.0 wt.%), the iron-bearing plagioclase

spectrum has a weak and broad absorption near 1250 nm. However, this absorption feature is easily masked by a few to several vol.% of mafic minerals in a mixture. Cheek and Pieters (2014) showed that as little as 2 vol.% of olivine or pyroxene completely masks this absorption. Nevertheless, implications of possible presence of large amounts of plagioclase in the interpreted spectral signature are discussed in this study.

Fundamental spectral parameters (band center (BC), band depth (BD) and band area (BA)) and derived parameters (integrated band depth (IBD), integrated band depth ratio (IBDR) and band area ratio (BAR)) are calculated in this study. All of them depict spectral variabilities among the VNIS measured in-situ spectra and therefore reveal mineral compositions of lunar regolith, which are of great significance to the interpretation of geological evolution. Band center (BC) is the wavelength position at the deepest absorption in a given wavelength range. BC positions of 1000 nm (BC1000) and 2000 nm (BC2000) absorption features are estimated in this study to differentiate between low-Ca pyroxenes (~ 900 nm and 1900 nm) and high-Ca pyroxenes (~ 1000 nm and 2200 nm). Band Depth (BD) represents the absorption strength at a particular wavelength. Integrated band depth (IBD) is the cumulative sum of the absorption strengths over a wavelength range. IBD1000 and IBD2000 that refer to integrated depths of the 1000 nm and 2000 nm absorption feature were introduced by Moon Mineralogy Mapper (M^3) science team, to characterize spectral variations modulated by Fe-

bearing mineral distribution and space weathering (Mustard et al., 2011). Integrated band depth ratio (IBDR) is defined as the ratio of IBD2000 to IBD1000. Band area (BA) is the area covered by an absorption feature in a given wavelength range. BA1000 and BA2000 refer to the area covered by the 1000 nm and 2000 nm absorptions respectively. They are used to derive band area ratio (BAR), which is the ratio of BA2000 to BA1000. As IBD is proportional to the band area of an absorption feature, BAR is calculated and discussed in this study. In accordance with the scheme adopted by the M³ team (Mustard et al., 2011) and considering the spectral resolution of VNIS data, the wavelength ranges used for calculating BA1000 and BA2000 are the same as that of IBD1000 (between 790 and 1310 nm) and IBD2000 (between 1660 and 2395 nm), respectively. Though they are wider than the actual absorption features owing to pyroxene and olivine, they provide a common baseline for comparing individual absorption features.

Before calculating spectral parameters, the spectrum has been spectrally subset to the region containing the absorption features of interest, and its continuum is removed, which helps minimizing influences from different observation backgrounds (e.g., various light conditions). The continuum is a convex hull fit over the top of a spectrum using straight-line segments that connect local spectra maxima. The first and last bands are on the hull, and their spectral values in the continuum-removed spectrum are equal to 1.0 (Clark and Roush, 1984). In addition, spectral slope for the visible wavelength region (VISslope), near-infrared wavelength region (NIRslope), shortwave infrared wavelength region (SWIRslope), and full-range spectral slope (FSslope) are calculated. The definitions and formulae of these parameters are stated in Supplementary Table 2.

3.4. MGM and NBSR analysis

The principle of the Modified Gaussian Model (MGM), originally proposed by Sunshine et al. (1990), is to deconvolve overlapping absorptions of mafic mineral spectra into their fundamental absorption components (Sunshine et al., 1990; Sunshine and Pieters, 1993). One gaussian function (characterized by band center, width and strength) or combination of multiple gaussian functions permits the identification of a mineralogical absorption band, indicative of the presence and composition of the predominant mafic minerals (Sunshine and Pieters, 1998). Based on Clénet et al. (2011) and Pinet et al. (2016), MGM is used here with 7 configurations to deconvolve overlapping absorptions of the Chang'e-4 VNIS spectrum. The numbers of gaussians in these configurations are listed in Supplementary Table 3. For example, The 'OL-OPX-CPX' configuration (last column in Supplementary Table 3) has 8 gaussians, including 1 for a strong absorption centered around 450 nm in the ultraviolet (UV) region (UV450), 3 for olivine (OL) absorptions (OL850, OL1050, OL1250), 2 for orthopyroxene (OPX) absorptions (OPX900, OPX1900), and 2 for clinopyroxene (CPX) absorptions (CPX1000, CPX2200) (Clénet et al., 2011, 2013). The continuum is fit by a second order polynomial with anchoring points adjusted on the local maxima along the spectrum and initial parameters of each gaussian are made on the basis of laboratory results (Clénet et al., 2011).

Kanner et al. (2007) found there is a strong positive relationship between normalized band strength ratio (NBSR) calculated from MGM derived band depths (also called absorption strengths) and the known mineral fractions in a two-pyroxene mixture. The concept of NBSR including olivine has been first introduced by Clénet et al. (2013). Five NBSR values are calculated in this study to predict the relative fractions of the mafic mineral mixtures, including NBSR(OL)_{1000 nm}, NBSR(OPX)_{1000 nm}, and NBSR(CPX)_{1000 nm} for the 1000 nm absorption region, NBSR(OPX)_{2000 nm} and

NBSR(CPX)_{2000 nm} for the 2000 nm absorption region. The formulae for them are stated in Supplementary Table 4.

4. Results and discussions

4.1. Lunar regolith reflectance properties

The 13 lunar regolith reflectance spectra observed by VNIS at the Chang'e-4 landing site has typical characteristics caused by space weathering. These in-situ measured reflectance spectra exhibit common features of increasing reflectance with increasing wavelength (reddening) (Fig. 2a). Two absorption features near 1000 nm and 2000 nm are discernible from continuum removed spectra (Fig. 2b). The averages and standard deviations of band depths for the 1000 nm and 2000 nm absorption features of the 13 regolith spectra are 0.12 ± 0.05 and 0.04 ± 0.01 , respectively, indicating the existence of pyroxene. The lack of significant 2000 nm absorptions in these regolith spectra indicates they have a very high degree of space weathering. A broad olivine absorption feature centered near 1050 nm also can be distinguished in continuum removed spectra. These in-situ spectral measurements are consistent with remote sensing observations of the SPA basin (Huang et al., 2018; Moriarty and Pieters, 2018).

All spectral slope values, regardless of type, have a general decreasing trend with Yutu-2 rover traversing away from the lander. This phenomenon is attributed to lander rocket plume, which blows away the uppermost mature regolith and exposes the less-mature regolith. Surface modifications by plumes, which changes reflectance within blast zone, have been documented by Surveyor, Luna, Apollo and Chang'e-3 on the Moon, and by Viking, Curiosity and especially Phoenix on Mars (Clegg et al., 2014). The full-range spectral slope from 450 nm to 2350 nm has a value of 0.07 ± 0.02 , the visible slope from 450 to 750 nm is 0.13 ± 0.05 , the near-infrared slope from 750 to 1500 nm is 0.09 ± 0.04 , and the shortwave infrared slope from 1500 to 2350 nm is 0.04 ± 0.01 . Both the mean and the standard variation of the slope value decrease gradually from visible to shortwave infrared wavelength region, which indicate that lander rocket exhaust effects has the largest influence on the visible wavelength region.

4.2. Spectral characteristics of regolith

Band area ratio (BAR) is a sensitive indicator for interpreting the spectral behavior of olivine–orthopyroxene mixtures, which is nearly independent of particle size and mineral composition (Cloutis et al., 1986). BAR contains information about the olivine abundance in olivine–pyroxene mixtures, which is inversely proportional to the abundance of olivine but increases linearly with the increase in pyroxene abundance (Cloutis et al., 1986). Gaffey et al. (1993) found the relationship between BC1000 and BAR can reduce the error caused by the presence of clinopyroxenes in the mixture. The low BAR values (0.27 ± 0.10) seen from BAR–BC1000 scatter plot (Fig. 3a) are in favor of a mixture of olivine–orthopyroxene and suggest a relatively high olivine/pyroxene ratio within minerals at the Chang'e-4 landing site (Clénet et al., 2011), though olivine absorptions are not obvious in the original spectra (Fig. 2a).

Extensive laboratory studies of terrestrial and synthetic pyroxenes provide the basis to correlate the 1000 nm and 2000 nm absorption positions with their chemical compositions. Orthopyroxene absorption bands (BC1000 and BC2000) shift to longer wavelengths with increasing amounts of iron and calcium and shift to shorter wavelengths with increasing magnesium, whereas clinopyroxene absorption bands shift to longer wavelengths with increasing calcium content and shift to shorter wavelengths with increasing iron (Adams, 1974; Cloutis et al., 1986; Klima et al., 2007;

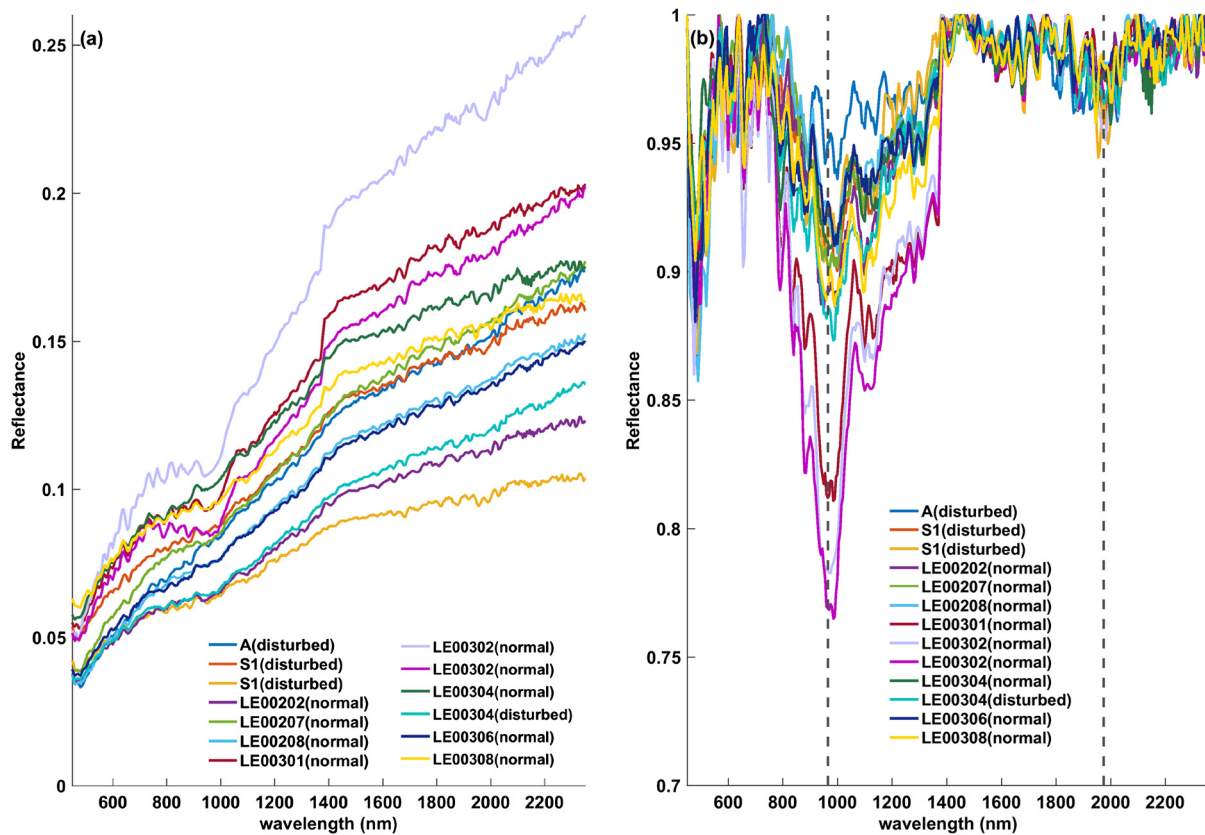


Fig. 2. Lunar regolith spectra observed by VNIS during the first three lunar days: (a) original; (b) continuum removed. The dashed lines in (b) are located at 965 nm and 1975 nm, respectively. The regolith state (normal or disturbed) of each observation is marked in the legend. The discontinuity in some spectra in this figure near 1400 nm is related to signals that arise from artifacts within the VNIS design.

Clénet et al., 2011). Thus, the relationship between band centers and iron and calcium content has been widely used to infer pyroxene composition from reflectance spectrum. The BC2000–BC1000 plot shows BC1000 varies from 949.8 nm to 998.1 nm (979.6 ± 15.5 nm), and BC2000 varies from 1935.3 nm to 2028.0 nm (1990.7 ± 35.0 nm) (Fig. 3b). Short 1000 nm and 2000 nm absorption centers indicate pyroxenes at Chang'e-4 landing site are chiefly Mg-rich orthopyroxenes (low-Ca pyroxene, LCP). These in-situ spectral observations are consistent with remote sensing observations from Moon Mineralogy Mapper and SELENE/Kaguya that suggests that Von Kármán crater (where Chang'e-4 landed) is situated in a zone dominated by abundant Mg-rich pyroxenes (Huang et al., 2018; Moriarty and Pieters, 2018).

4.3. MGM modeling of a rock spectrum

In addition to regolith, the spectrum of a 20-centimeter rock fragment was observed by VNIS at 1.2 meters distance on the third lunar day. VIS/NIR image with a spatial resolution of 1 mm/pixel shows it has much higher albedo compared to the surrounding regolith (Fig. 4a). It is really quite hard to figure out whether this rock fragment is crystallized or non-crystallized at a sub-cm or mm scale, either from panoramic camera image or from navigation camera image (Supplementary Fig. 2), or from VIS/NIR image (Fig. 4a). A small to even medium-grained textures can be seen dimly from the VIS/NIR image which has the highest resolution (1 mm/pixel), indicating the rock is likely plutonic. It is conservatively estimated that the rock fragment lacks discernible coarse-grained textures (>5 mm crystals visible to naked eyes).

The rock spectrum has a low BAR value of 0.17, and the 1000 nm and 2000 nm mafic mineral absorption features are obvious (Fig. 4b). Because fitting with other configurations either have ex-

trême weak or even positive absorption strengths (e.g., fitting with 'OL-CPX' configuration produces a positive absorption strength for olivine-related absorption at 1050 nm, Supplementary Fig. 3), or have unreasonable wavelength centers/widths (e.g., fitting with 'OL' configuration produces an unreasonable wavelength center for olivine-related absorption at 1000 nm, Supplementary Fig. 4), or have relative large fitting errors (e.g., fitting with 'OPX-CPX' configuration produces a relative large error, Supplementary Fig. 5), MGM fitting with 'OL-OPX-CPX' configuration (initial and final fitting parameters are listed in Supplementary Table 5) provides the optimal modeling in terms of mineral detection for this rock spectrum (Fig. 5). Then, in order to predict Mg number (Fo#) (Sunshine and Pieters, 1998), the MGM modeled three olivine-related band centers estimates are fit to a laboratory derived compositional trend line by finding the least error (Sunshine and Pieters, 1998). However, the precise determination of the overall uncertainty on Mg number is not an easy task (Isaacson and Pieters, 2010; Pinet et al., 2018, 2019). Relying on these studies, a first order estimate of the uncertainty is likely to be on the order of 10–15% Fo# range. Accordingly, depending on the minimization used, the predicted olivine Fo# appears to be in the range 80–84, with an uncertainty on the order of 10, pointing at a Mg-rich composition (forsterite). It should be noted here that the complex olivine absorption feature not only varies with the iron content but also with grain size and abundance. As demonstrated by Clénet et al. (2011), a forsterite with very large grains and a fayalite with smaller grains may have similar spectral features. Everything considered, this high Fo# value is very tentative here and should thus be treated with caution.

NBSR values (Table 1) for the 1000 nm absorption feature predict clinopyroxene accounts for the largest fraction, followed by orthopyroxene and then olivine (olivine: orthopyroxene: clinopy-

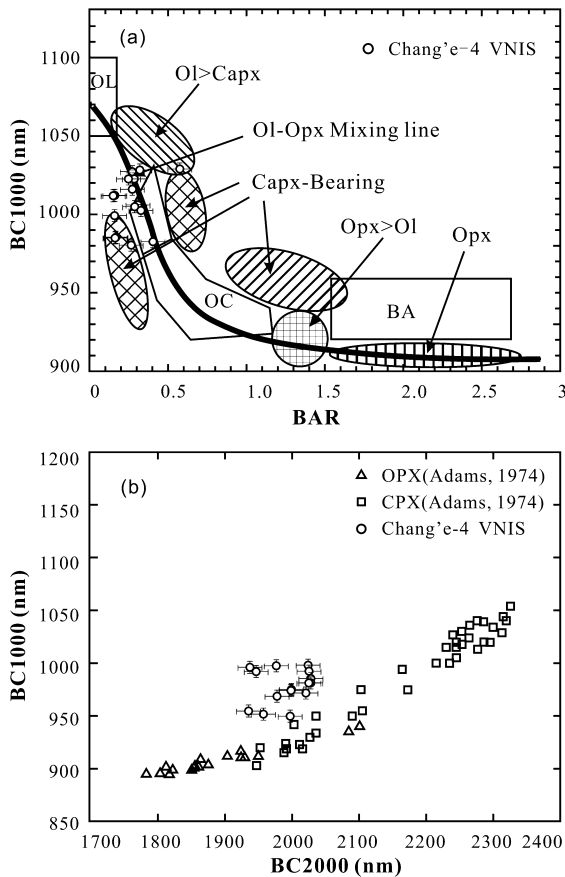


Fig. 3. Scatter plots of spectral parameters. (a) BAR-BC1000; (b) BC2000-BC1000. Reference compositional groups are from Cloutis et al. (1986) and Adams (1974), respectively. The error bars in each plot represent a first-order approximation for the uncertainty determined by the law of propagation of uncertainty. Here OC – ordinary chondrites and BA – pyroxene dominated basaltic achondrites.

roxene is 25%: 33%: 42%). NBSR values for the 2000 nm absorption features also predict clinopyroxene has a bit higher fraction than orthopyroxene (orthopyroxene: clinopyroxene is 43%: 57%), indicating self-consistent in mineral fractions. The mineral composition and fraction of the rock fragment predicted from MGM fitting and NBSR values are in agreement with that inferred from the spectral parameter scatter plots for the regolith, indicating the rock fragment may have a high probability that it originates from the same material as the surrounding lunar regolith.

Lunar Reconnaissance Orbiter Diviner observations show that thermal infrared (TIR) emissivity spectra at a spatial resolution of

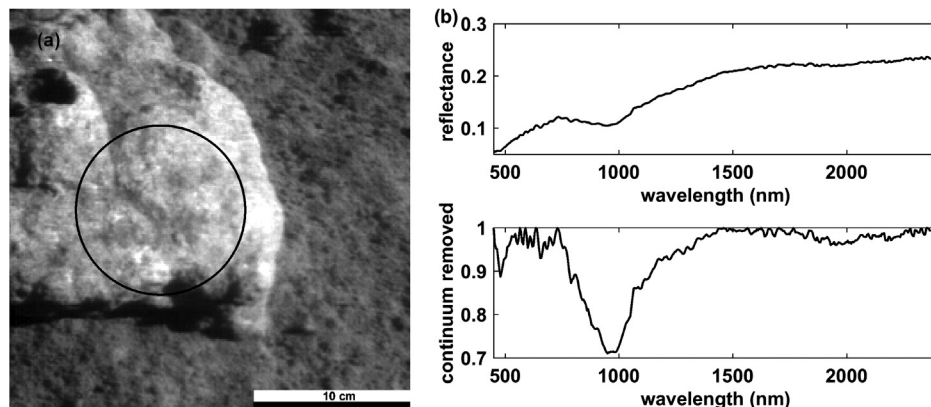


Fig. 4. A rock fragment detected along the Yutu-2 rover traverse. (a) VIS/NIR image (1 mm/pixel) @ 750 nm, the black circle corresponds to the field of view of the SWIR spectrometer. (b) Rock spectrum (top: original, bottom: continuum removed).

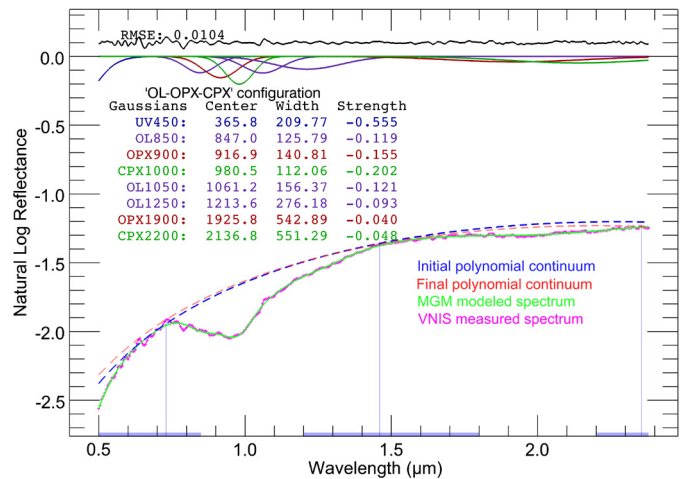


Fig. 5. Rock spectrum modeled with 'OL-OPX-CPX' configuration by MGM.

Table 1
NBSR values of the rock spectrum.

NBSR [*]	1000 nm absorption			2000 nm absorption	
	NBSR(OL)	NBSR(OPX)	NBSR(CPX)	NBSR(OPX)	NBSR(CPX)
Value ^{**}	0.25	0.33	0.42	0.43	0.57

^{*} The definitions of the NBSR are stated in supplementary material.

^{**} These values represent relative fractions.

~250 m/pixel indicate mixtures of plagioclase and olivine (Arnold et al., 2016) where olivine-rich sites (e.g., locations around the SPA basin) have been identified with visible to near infrared (VNIR) observations at a resolution of ~500 m/pixel (Yamamoto et al., 2010). The discrepancy between this study and previous work was probably caused by: (1) different observation methods (orbital vs. in-situ); (2) different observation bands (TIR vs. VNIR); (3) great resolution differences (e.g., non-imaging single-pixel vs. hundreds of meters per pixel). In addition, because of minerals' overlapping spectral absorption features (e.g., mafic minerals and plagioclase), large amounts of plagioclase in the rock (if exists) can be masked in the spectral signature of the olivine- and pyroxene-dominated spectrum that are being interpreted here. Considering this scenario and above stated grain size effects, it should also be noted that further MGM modeling experiments should be carried out to better understand the influence of the possible presence of large amounts of plagioclase and mineral grain sizes on estimating relative mineral fractions and assessing olivine compositions (Pinet, 2019), which has huge implications for the origin of the VNIS ob-

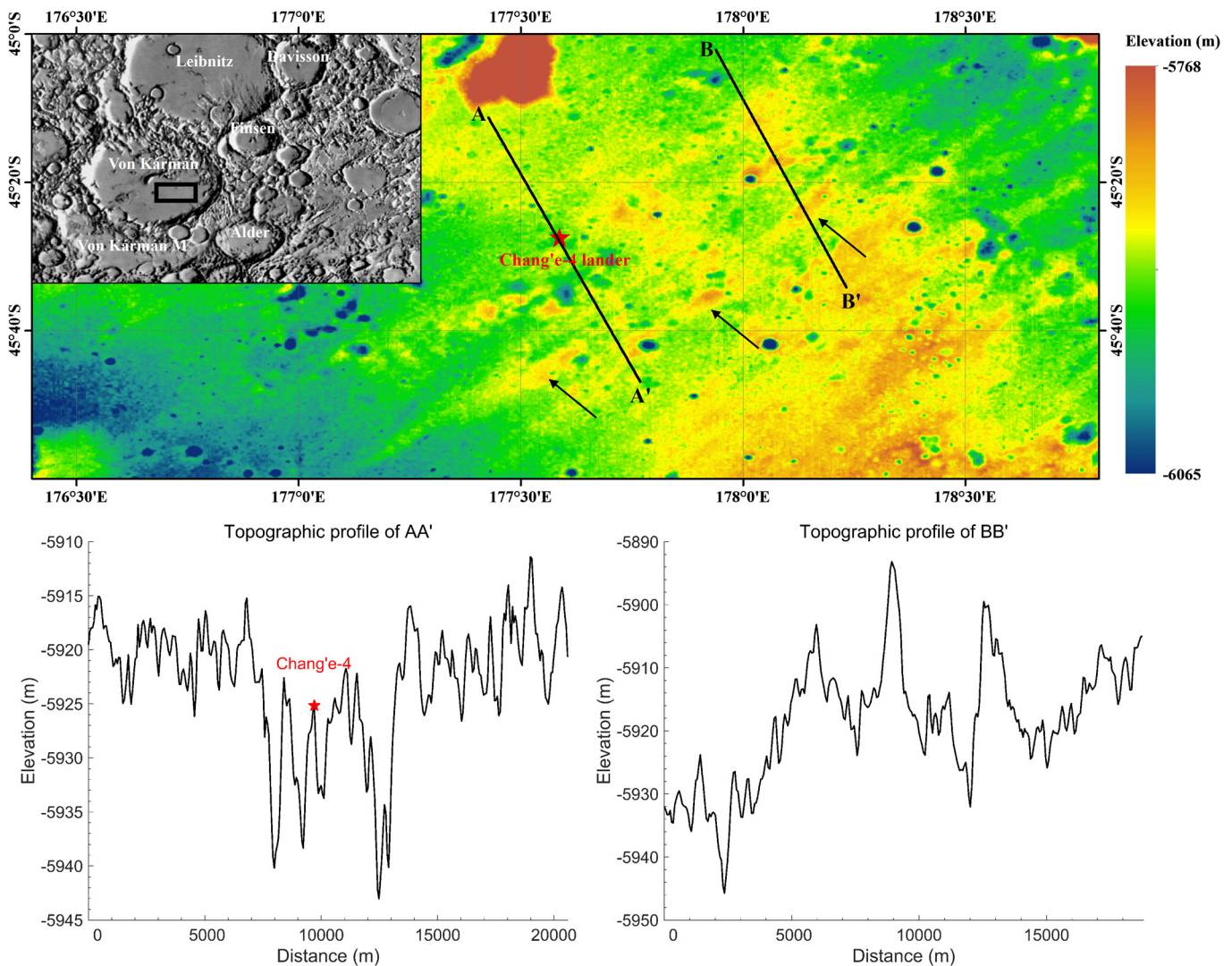


Fig. 6. Top panel: Elevation map at Chang'e-4 landing site. Black arrows indicate the NE-SW trend features and black rectangle in the shaded relief inset in the upper left indicates the location of the elevation map within the Von Kármán crater. Bottom panel: Topographic profile of A-A' that crosses the Chang'e-4 landing site, and that of B-B' shows topographic variations with notable intervals.

served materials (e.g., large amounts of plagioclase in a rock would completely change the type of rock being observed, which indicate the rock would not be expected to originate from the mantle, but rather likely from the crust).

4.4. Origin of the VNIS observed regolith and rock fragment

Obvious NE-SW trending linear features cut across this region, which is radiated from the relatively young ~ 72.98 km diameter Finsen crater (Fig. 6). Topographic profile extracted from an improved lunar digital elevation model (DEM) SLDEM2015 (Barker et al., 2016), which has a resolution of 512 pixels per degree (~ 42 m/pixel at the Chang'e-4 landing site), shows Chang'e-4 landed on these NE-SW trending elevated streaks which have an interval of about 3 km (Fig. 6). SELENE/Kaguya Multiband Imager (MI) reflectance mosaic and false color composite images show Chang'e-4 landed on the low albedo regions (Supplementary Fig. 6), which are likely ejecta materials (Supplementary Fig. 7). Therefore, the Chang'e-4 landing site is in the area affected by ejecta materials coming from Finsen crater, which is 370 km away from the center of the transient cavity of SPA basin (Potter et al., 2012). The local mare basalt deposits at the Chang'e-4 landing site should be extensively mixed with or covered by ejecta materials from Fin-

sen crater. Ling et al. (2018) divided the mare region within Von Kármán crater into two units: low-Ti unit (LT, 3 wt.% $>$ $\text{TiO}_2 >$ 1.5 wt.%) and Finsen ejecta unit (FE, $\text{TiO}_2 <$ 1.5 wt.%). Chang'e-4 just landed at the FE unit (1.42 ± 0.24 wt.% TiO_2). Combined with above information and the rock fragment may have a plutonic origin, the VNIS observed Mg-rich olivine (Fo# 80-84 \pm 10) and LCP-bearing regolith and rock fragment are essentially lunar deep-seated materials excavated from the nearby Finsen crater at a depth $Hexc$ of 3.65–4.74 km.

The SPA basin forming impact event had substantially thinned the lunar crust through excavation and the event can generate an impact melt pond within the basin. Hence, the sources of these VNIS observed deep-seated materials may originate from: (1) the lunar lower crust; (2) the lunar upper mantle; (3) a differentiated melt pool. Previous works have suggested that perhaps only the lower crust was exposed during the SPA impact event if it was an oblique impact (Pieters et al., 2001; Garrick-Bethell and Zuber, 2009), however, recent numerical modeling works suggest that mantle material should be excavated by the SPA forming impact even if it's an very oblique impact (e.g., impact at an angle of 20°) (Melosh et al., 2017; Zhu et al., 2018). Melosh et al. (2017) proposed the SPA basin should have exposed the Moon's upper mantle materials, which is dominated by LCP. Remote sensing observations

suggested the presence of a thick LCP-bearing layer in the SPA sub-surface (Pieters et al., 1997). LCP-bearing materials indeed have been detected using orbital spectral data at many central peaks within SPA basin, including Finsen crater (Moriarty et al., 2013). Therefore, the VNIS observed Mg-rich LCP-bearing lunar regolith and rock fragment (with high Fo# for the olivine mineral) are very likely to be lunar mantle materials excavated from nearby Finsen crater. Alternatively, most materials within the SPA basin are melted due to impact-produced high pressure (Hurwitz and Kring, 2014; Vaughan and Head, 2014). However, the definitive identification of SPA derived impact melt on the basin floor, either by remote sensing or via photogeology, is extremely difficult due to the number of subsequent impacts and volcanic activities (Petro, 2011). It cannot be excluded here that the VNIS observed local materials might originate from the lower base of a differentiated melt pool. As the SPA basin has not been sampled either by previous lunar sample return missions (Apollo, Luna) or by lunar meteorites, a definitive answer to the sources of VNIS observed materials can only be addressed in the future through detailed analysis on returned samples.

5. Conclusion

The first in-situ spectral observations on the lunar farside reveal the regolith at the Chang'e-4 landing site has a relative high olivine/pyroxene ratio; with the pyroxene being mainly Mg-rich LCP. The observed rock fragment has a composition similar to that of the surrounding regolith, with a rather Mg-rich olivine composition (Fo# 80–84 \pm 10). Topographic and geologic analysis show Chang'e-4 just landed on the ejecta of nearby \sim 72.98 km diameter Finsen crater. Though originating from the lower base of a differentiated melt pool cannot be excluded here, the VNIS observed lunar regolith and rock fragment are very likely to be lunar upper mantle materials excavated from nearby Finsen crater. The in-situ spectral observations confirm previous orbital observations and numerical impact simulations in the SPA basin, and complement the initial results recently reported by Li et al. (2019) that Chang'e-4 may have discovered material from the Moon's mantle.

Acknowledgements

The authors gratefully thank the whole Chang'e-4 team for making the mission a great success and providing the data. This research is supported by Key Research Program of the Chinese Academy of Sciences (Grant No. XDPB11), National Natural Science Foundation of China (grant No. 41702354 and 41941003), Macau Young Scholars Program (grant No. AM201902), and Science and Technology Development Fund of Macau (grant No. 131/2017/A3). Constructive reviews by Patrick Pinet and an anonymous reviewer improved the quality of this manuscript substantially, and are greatly appreciated.

Appendix A. Supplementary material

Supplementary material related to this article can be found online at <https://doi.org/10.1016/j.epsl.2019.115829>.

References

- Adams, J.B., 1974. Visible and near-infrared diffuse reflectance spectra of pyroxenes as applied to remote sensing of solid objects in the solar system. *J. Geophys. Res.* 79, 4829–4836.
- Arnold, J.A., Glotch, T.D., Lucey, P.G., Song, E., Thomas, I.R., Bowles, N.E., Greenhagen, B.T., 2016. Constraints on olivine-rich rock types on the Moon as observed by Diviner and M3: implications for the formation of the lunar crust. *J. Geophys. Res., Planets* 121, 1342–1361.
- Barker, M.K., Mazarico, E., Neumann, G.A., Zuber, M.T., Haruyama, J., Smith, D.E., 2016. A new lunar digital elevation model from the Lunar Orbiter Laser Altimeter and SELENE Terrain Camera. *Icarus* 273, 346–355.
- Cheek, L.C., Pieters, C.M., 2014. Reflectance spectroscopy of plagioclase-dominated mineral mixtures: implications for characterizing lunar anorthosites remotely. *Am. Mineral.* 99, 1871–1892.
- Clark, R.N., Roush, T.L., 1984. Reflectance spectroscopy: quantitative analysis techniques for remote sensing applications. *J. Geophys. Res.* 89, 6329–6340.
- Clegg, R.N., Jolliff, B.L., Robinson, M.S., Hapke, B.W., Plescia, J.B., 2014. Effects of rocket exhaust on lunar soil reflectance properties. *Icarus* 227, 176–194.
- Cl  net, H., Pinet, P., Ceuleneer, G., Daydou, Y., Heuripeau, F., Rosemberg, C., Bibring, J.P., Bellucci, G., Altieri, F., Gondet, B., 2013. A systematic mapping procedure based on the Modified Gaussian Model to characterize magmatic units from olivine/pyroxenes mixtures: application to the Syrtis Major volcanic shield on Mars. *J. Geophys. Res.* 118, 1632–1655.
- Cl  net, H., Pinet, P., Daydou, Y., Heuripeau, F., Rosemberg, C., Baratoux, D., Chevrel, S., 2011. A new systematic approach using the modified Gaussian model: insight for the characterization of chemical composition of olivines, pyroxenes and olivine–pyroxene mixtures. *Icarus* 213, 404–422.
- Cloutis, E.A., Gaffey, M.J., Jackowski, T.L., Reed, K.L., 1986. Calibrations of phase abundance, composition, and particle size distribution for olivine-orthopyroxene mixtures from reflectance spectra. *J. Geophys. Res., Solid Earth* 91, 11641–11653.
- Coddington, O., Lean, J., Pilewskie, P., Snow, M., Lindholm, D., 2016. A solar irradiance climate data record. *Bull. Am. Meteorol. Soc.* 97, 1265–1282.
- Gaffey, M.J., Bell, J.F., Brown, R.H., Burbine, T.H., Piatek, J.L., Reed, K.L., Chaky, D.A., 1993. Mineralogical variations within the S-type asteroid class. *Icarus* 106, 573–602.
- Garrick-Bethell, I., Zuber, M.T., 2009. Elliptical structure of the lunar South Pole-Aitken basin. *Icarus* 204, 399–408.
- He, Z., Wang, B.Y., Lv, G., Li, C.L., Yuan, L.Y., Xu, R., Chen, K., Wang, J., 2014. Visible and near-infrared imaging spectrometer and its preliminary results from the Chang'e 3 project. *Rev. Sci. Instrum.* 85, 083104.
- Huang, J., Xiao, Z., Flahaut, J., Martinot, M., Head, J., Xiao, X., Xie, M., Xiao, L., 2018. Geological characteristics of von K  rman Crater, Northwestern South Pole-Aitken Basin: Chang'e-4 landing site region. *J. Geophys. Res., Planets* 123, 1684–1700.
- Hurwitz, D.M., Kring, D.A., 2014. Differentiation of the South Pole-Aitken basin impact melt sheet: Implications for lunar exploration. *J. Geophys. Res., Planets* 119, 1110–1133.
- Isaacson, P.J., Pieters, C.M., 2010. Deconvolution of lunar olivine reflectance spectra: implications for remote compositional assessment. *Icarus* 210, 8–13.
- Jia, Y., Zou, Y., Ping, J., Xue, C., Yan, J., Ning, Y., 2018. The scientific objectives and payloads of Chang'e-4 mission. *Planet. Space Sci.* 162, 207–215.
- Kanner, L.C., Mustard, J.F., Gendrin, A., 2007. Assessing the limits of the modified Gaussian model for remote spectroscopic studies of pyroxenes on Mars. *Icarus* 187, 442–456.
- Klima, R.L., Pieters, C.M., Dyar, M.D., 2007. Spectroscopy of synthetic Mg-Fe pyroxenes I: spin-allowed and spin-forbidden crystal field bands in the visible and near-infrared. *Meteorit. Planet. Sci.* 42, 235–253.
- Lawrence, D.J., Feldman, W.C., Barraclough, B.L., Binder, A.B., Elphic, R.C., Maurice, S., Thomsen, D.R., 1998. Global elemental maps of the Moon: the lunar prospector gamma-ray spectrometer. *Science* 281, 1484–1489.
- Li, C., Liu, D., Liu, B., Ren, X., Liu, J., He, Z., Zuo, W., Zeng, X., Xu, R., Tan, X., Zhang, X., Chen, W., Shu, R., Wen, W., Su, Y., Zhang, H., Ouyang, Z., 2019. Chang'e-4 initial spectroscopic identification of lunar far-side mantle-derived materials. *Nature* 569, 378–382.
- Ling, Z., Jolliff, B.L., Liu, C.Q., Bi, X.Y., Liu, L., Qiao, L., Zhang, J., Fu, X., Liu, J., 2018. Composition, mineralogy, and chronology of mare basalts in von K  rman Crater: a candidate landing site of Chang'e-4. In: 49th Lunar and Planetary Science Conference. The Woodlands, Texas, p. 1939.
- Liu, B., Liu, J.-Z., Zhang, G.-L., Ling, Z.C., Zhang, J., He, Z., Yang, B.-Y., Zou, Y.-L., 2013. Reflectance conversion methods for the VIS/NIR imaging spectrometer aboard the Chang'e-3 lunar rover: based on ground validation experiment data. *Res. Astron. Astrophys.* 13, 862–874.
- Melosh, H.J., 1989. *Impact Cratering: A Geologic Process*. Oxford University Press.
- Melosh, H.J., Kendall, J., Horgan, B., Johnson, B.C., Bowling, T., Lucey, P.G., Taylor, G.J., 2017. South Pole-Aitken basin ejecta reveal the Moon's upper mantle. *Geology* 45, 1063–1066.
- Miljkovic, K., Wieczorek, M.A., Collins, G.S., Solomon, S.C., Smith, D.E., Zuber, M.T., 2015. Excavation of the lunar mantle by basin-forming impact events on the Moon. *Earth Planet. Sci. Lett.* 409, 243–251.
- Moriarty, D.P., Pieters, C.M., 2018. The character of South Pole-Aitken Basin: patterns of surface and subsurface composition. *J. Geophys. Res., Planets* 123, 729–747.
- Moriarty, D.P., Pieters, C.M., Isaacson, P.J., 2013. Compositional heterogeneity of central peaks within the South Pole-Aitken Basin. *J. Geophys. Res., Planets* 118, 2310–2322.
- Mustard, J.F., Pieters, C.M., Isaacson, P.J., Head, J.W., Besse, S., Clark, R.N., Klima, R.L., Petro, N.E., Staid, M.I., Sunshine, J.M., 2011. Compositional diversity and geologic insights of the Aristarchus crater from Moon Mineralogy Mapper data. *J. Geophys. Res., Planets* 116.

- Petro, N.E., 2011. Volume of impact melt generated by the formation of the South Pole-Aitken Basin. In: Annual Meeting of the Lunar Exploration Analysis Group. Houston, Texas.
- Pieters, C.M., Head III, J.W., Gaddis, L., Jolliff, B., Duke, M., 2001. Rock types of South Pole-Aitken basin and extent of basaltic volcanism. *J. Geophys. Res., Planets* 106, 28001–28022.
- Pieters, C.M., Tompkins, S., Head, J.W., Hess, P.C., 1997. Mineralogy of the Mafic Anomaly in the South Pole-Aitken Basin: implications for excavation of the lunar mantle. *Geophys. Res. Lett.* 24, 1903–1906.
- Pinet, P., 2019. The Moon's mantle unveiled. *Nature* 569, 338–339.
- Pinet, P.C., Chevrel, S.D., Daydou, Y.H., 2018. Characterization of the olivine/plagioclase mineralogy at Copernicus Crater from MGM deconvolution of M3 observations. In: 49th Lunar and Planetary Science Conference. The Woodlands, Texas, LPI Contrib. No. 2083.
- Pinet, P.C., Chevrel, S.D., Daydou, Y.H., 2019. Reassessing the relationship between olivine composition and reflectance spectroscopy from advanced MGM deconvolution. In: 50th Lunar and Planetary Science Conference. The Woodlands, Texas.
- Pinet, P.C., Glenadel-Justaut, D., Daydou, Y., Ceuleneer, G., Gou, S., Launeau, P., Chevrel, S., Carli, C., 2016. MGM deconvolution of complex mafic mineralogy rock slab spectra from visible-near infrared imaging spectroscopy: implications for the characterization of the terrestrial ocean crust and of the lunar crust. In: The 8th Workshop on Hyperspectral Image and Signal Processing: Evolution in Remote Sensing. WHISPERS, Los Angeles, USA.
- Potter, R.W.K., Collins, G.S., Kiefer, W.S., McGovern, P.J., Kring, D.A., 2012. Constraining the size of the South Pole-Aitken basin impact. *Icarus* 220, 730–743.
- Schultz, P.H., Crawford, D.A., 2011. Origin of nearside structural and geochemical anomalies on the Moon. *Geol. Soc. Am. Spec. Pap.* 477, 141–159.
- Spudis, P.D., Gillis, J.J., Reisse, R.A., 1994. Ancient multiring basins on the Moon revealed by Clementine Laser Altimetry. *Science* 266, 1848–1851.
- Stuart-Alexander, D.E., 1978. Geologic map of the central far side of the Moon. *IMAP* 1047.
- Sunshine, J.M., Pieters, C.M., 1993. Estimating modal abundances from the spectra of natural and laboratory pyroxene mixtures using the modified Gaussian model. *J. Geophys. Res.* 98, 9075–9087.
- Sunshine, J.M., Pieters, C.M., 1998. Determining the composition of olivine from reflectance spectroscopy. *J. Geophys. Res.* 103, 13675–13688.
- Sunshine, J.M., Pieters, C.M., Pratt, S.F., 1990. Deconvolution of mineral absorption bands – an improved approach. *J. Geophys. Res.* 95, 6955–6966.
- Vaughan, W.M., Head, J.W., 2014. Impact melt differentiation in the South Pole-Aitken basin: some observations and speculations. *Planet. Space Sci.* 91, 101–106.
- Wieczorek, M.A., Neumann, G.A., Nimmo, F., Kiefer, W.S., Taylor, G.J., Melosh, H.J., Phillips, R.J., Solomon, S.C., Andrews-Hanna, J.C., Asmar, S.W., Konopliv, A.S., Lemoine, F.G., Smith, D.E., Watkins, M.M., Williams, J.G., Zuber, M.T., 2013. The crust of the Moon as seen by GRAIL. *Science* 339, 671–675.
- Wu, W., Li, C., Zuo, W., Zhang, H., Liu, J., Wen, W., Su, Y., Ren, X., Yan, J., Yu, D., Dong, G., Wang, C., Sun, Z., Liu, E., Yang, J., Ouyang, Z., 2019. Lunar farside to be explored by Chang'e-4. *Nat. Geosci.* 12, 222–223.
- Wu, Y., Wang, Z., Cai, W., Lu, Y., 2018. The absolute reflectance and new calibration site of the Moon. *Astron. J.* 155, 213.
- Yamamoto, S., Nakamura, R., Matsunaga, T., Ogawa, Y., Ishihara, Y., Morota, T., Hirata, N., Ohtake, M., Hiroi, T., Yokota, Y., Haruyama, J., 2010. Possible mantle origin of olivine around lunar impact basins detected by SELENE. *Nat. Geosci.* 3, 533.
- Yamamoto, S., Nakamura, R., Matsunaga, T., Ogawa, Y., Ishihara, Y., Morota, T., Hirata, N., Ohtake, M., Hiroi, T., Yokota, Y., Haruyama, J., 2012. Olivine-rich exposures in the South Pole-Aitken Basin. *Icarus* 218, 331–344.
- Zhu, M.-H., Wünnemann, K., Morbidelli, A., Artemieva, N.A., 2018. South Pole-Aitken basin may contribute insignificantly to the late accretion of the Moon. In: 49th Lunar and Planetary Science Conference, p. 1955.